Cell Reports
Physical Science

CellPress

Article

High-Frequency Water Vapor Sorption Cycling Using Fluidization of Metal-Organic Frameworks

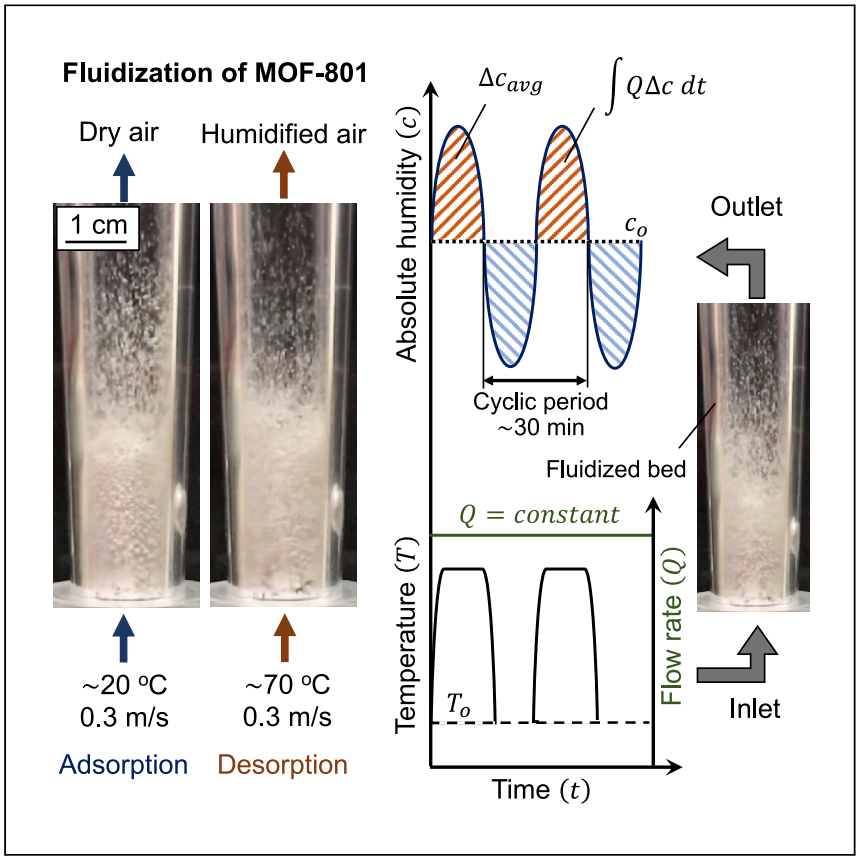

Terzis et al. report high-frequency water vapor sorption cycling using fluidization of metal-organic frameworks (MOFs). This arrangement enables the completion of water vapor adsorption and desorption phases within minutes, dramatically increasing cycle frequency, and thus, water vapor harvesting rates per day normalized by the MOF mass.

Alexandros Terzis, Ashwin Ramachandran, Kecheng Wang, Mehdi Asheghi, Kenneth E. Goodson, Juan G. Santiago

juan.santiago@stanford.edu

HIGHLIGHTS

High-frequency water vapor sorption cycling using fluidized metal-organic frameworks

Fluidization results in small distances over which mass and heat need to diffuse

Continuously cycled operation in excess of 75% of MOF-801 uptake capacity

Moisture harvesting rates on the order of 10 L/day/kg of MOF-801

Terzis et al., Cell Reports Physical Science *1*, 100057
May 20, 2020
https://doi.org/10.1016/j.xcrp.2020.100057

Cell Reports
Physical Science

CellPress
OPEN ACCESS

Article

High-Frequency Water Vapor Sorption Cycling Using Fluidization of Metal-Organic Frameworks

Alexandros Terzis,[1] Ashwin Ramachandran,[1] Kecheng Wang,[2] Mehdi Asheghi,[1] Kenneth E. Goodson,[1] and Juan G. Santiago[1,3,*]

SUMMARY

The productivity of continuously cycled atmospheric water harvesting methods using metal-organic frameworks (MOFs) has been limited by a lack of scalable designs and robust MOF form factors compatible with rapid heat and mass transport. Explored here is the fluidization of MOF-801 powder in its native particulate form as a water vapor sorption unit. Fluidization results in a very high sorbent-air interface area and small distances over which mass diffusion must occur. This arrangement enables adsorption and desorption cycling with periods of 26 and 36 min at, respectively, 18% and 39% relative humidity (RH) with ~80% of MOF-801 uptake capacity. This results in dynamic steady-state operation water vapor harvesting rates of 0.33 L/h/kg$_{MOF}$ at 18% RH (40 cycles per day at 22°C) and 0.52 L/h/kg$_{MOF}$ at 39% RH (55 cycles per day at 23.5°C). The measurements may have direct application to water harvesting systems.

INTRODUCTION

Atmospheric water harvesting (AWH) is an important alternative water resource due to the abundance of water vapor in the atmosphere, which constitutes a resource equivalent to ~15% of global freshwater in rivers and lakes.[1] Among different AWH methods, sorption-based techniques are well known[2] and recently gathered scientific attention with the development of metal-organic frameworks (MOFs). MOFs are a new class of well-defined crystalline materials that consist of metal ions or clusters bonded to organic ligands to form multi-dimensional coordinated structures on the molecular scale.[3,4] Depending upon the MOF material nature, the voids of these porous networks can be chemically tuned to act as depositories wherein large amounts of specific gas species (e.g., water for AWH) can be adsorbed, stored, and released for further use.

The design point of an atmospheric water harvester depends on the sorbent's adsorption isotherm, and for MOFs, a proper selection from a huge database[5–8] will yield the water harvesting potential based on ambient temperature and relative humidity (RH). A recent proof-of-concept device demonstrated the possibility of harvesting moisture and producing liquid water at 20% RH with a zirconium-based MOF, MOF-801.[9] MOF-801, shaped in a thin packed bed geometry, was exposed to ambient temperature to adsorb moisture during the nighttime and then solar heated during the daytime to release the captured water within a fixed-volume box. The increased water vapor capacity in the device drove dew condensation and droplet formation. Similar devices[10,11] were tested in the Arizona desert (USA), and showed water production of 0.25 and 0.1 L/kg$_{MOF}$/day with the

[1]Department of Mechanical Engineering, Stanford University, Stanford, CA 94305, USA

[2]Department of Materials Science and Engineering, Stanford University, Stanford, CA 94305, USA

[3]Lead Contact

*Correspondence: juan.santiago@stanford.edu

https://doi.org/10.1016/j.xcrp.2020.100057

assistance of an external condenser[10] or by using only natural cooling.[11] At the same time, a significant effort was made to develop materials with exceptional water uptake capacities.[12,13]

The current high cost of MOF-type adsorbents, however, strongly implies that water capture methods should be designed to maximize the system water productivity normalized by the MOF mass. Here, we advocate that this necessarily implies a multi-cycle operation of MOF adsorbent per day. As previously reported,[9] continuous cyclic operation of a 1-mm-thick MOF-801 with a packing porosity of 0.7 could typically allow 8 cycles per day, which can yield 0.9 L/m^2 or 2.8 L/kg$_{MOF}$/day at 20% RH. Higher-frequency operations can be achieved only with more rapid sorption dynamics. One important advancement in the area is the development of an aluminum-based MOF, MOF-303, which has been shown in small-scale laboratory experiments to perform adsorption and desorption phases within minutes.[11,14] In the latter work, continuous cyclic operation of several MOF-303 layers of 3-mm thickness and 0.7 packing porosity provided an average of 8.3 (unsaturated) cycles per day over a 72-h period.[14] The device was powered by electrical heater strips, and additional fans were used to drive an airstream through the adsorbent cell and then to an external condenser, generating 1.3 L/kg$_{MOF}$/day at laboratory conditions (32% RH, 27°C) and 0.7 L/kg$_{MOF}$/day in the Mojave Desert (10% RH, 27°C). We attribute the current limitations on operation frequency to the very large diffusion time scales of the packed bed sorbent geometries, which result in multi-hour adsorption and desorption times,[9] and often partially saturated adsorbents, even if the packed bed of MOFs is adjacent to a forced convective flow.[14]

Much of the work around implementation and scaling up of MOF material applications has been on the formation of porous solid form factors, which are then integrated into mass exchange units. These porous solid form factors are typically achieved with the use of additional materials that act as binders or by packing or mechanically confining the powder using supporting mesh structures.[15–20] These form factors may be convenient for assembly and analysis, but they drastically reduce the adsorption rate and can lower the capacity of the porous solid structures—both of which negatively affect mass and heat transport. Furthermore, the sorption dynamics of MOFs is very sensitive to pressure-shaping processes.[21] The transfer of species into and out of the adsorbents in such porous solids is hindered by slow transport through the interstitial spaces between grains or the diffusion into and out of larger grains and/or grain agglomerates. In many cases, there is no appreciable advection of mixture through interstitial spaces, and the transport can be additionally limited by molecular diffusion.[9]

To date, the specific productivity of sorption-based atmospheric water harvesters operated by MOFs has been limited to on the order of 0.1–1.3 L/kg$_{MOF}$/day.[9–11,14] We attribute this severe limitation to the single daily cycle operation and/or the low characteristic operating frequencies that have been used given the current MOF form factors. Here, we propose a fluidized bed as a form factor, which is a scalable technology[22] that is widely used in industrial applications, such as the petrochemical industry,[23] and for biomass gasification.[24] Fluidization has been proposed as a method to activate and shape MOF materials for CO_2 capturing applications.[25,26] However, fluidized MOF systems have not been used for adsorption-desorption cycling, and we are aware of no work reporting experimental measurements of sorption dynamics of any kind in a MOF fluidized bed. Water vapor adsorption and desorption has also been shown in fluidized beds of silica gel materials with applications to air-conditioning systems.[27,28] The latter studies, however,

have not demonstrated the cycling of sorption and have not demonstrated dynamic steady-state operation of the sorption process. With the fluidization of MOFs, we dramatically increase the productivity of the sorption component of a water vapor capture system by achieving exceptionally high rates of mass transfer and operational frequencies. As we discuss in the Results, this is achieved by increasing the surface area of adsorbent exposed to an airstream while simultaneously decreasing characteristic length scales over which diffusion must act for mass exchange. In particular, we experimentally demonstrate a fast response operation of fluidized MOF-801 at >75% of its uptake capacity, capable of yielding water vapor harvesting rates an order of magnitude higher than any existing technology. This is possible by the achievement of 40 and 55 adsorption-desorption cycles per day at only 18% and 39% RH, respectively.

RESULTS

Fluidized MOF Powder Enables High-Frequency Adsorption-Desorption Cycling

A fluidized bed is a system in which a continuous fluid phase (typically gas) is flowed through a vertical vessel containing solid particulates.[29] The interaction of the continuous fluid phase with the particulates causes the particulates to trade momentum with the continuous fluid phase, causing the system to move and mix. The entire fluid-solid mixture is "fluidized" when the drag and buoyancy forces balance gravity and the total system adopts some properties of a fluid (e.g., continuously deforming under shear stress). A schematic representation of a fluidized adsorbent cell for AWH applications is shown in Figure 1. At the inlet of the fluidized bed, the airstream temperature is periodically varied between cold (ambient) and hot conditions to drive, respectively, moisture adsorption and desorption into and out of the adsorbent. Subsequently, continuous cycled water vapor harvesting can be obtained at the exit of the fluidized bed during the regeneration process of the sorbent. The requirement for heating is compatible with low-grade waste heat, and the system has potential for 24-h operation.

In their native powder form, fine adsorbent powders such as MOFs are characterized as "cohesive particles," based on the Geldart fluidization diagram.[29] Due to their small single crystal length scales, typically varied from a fraction to a few microns, interparticle forces caused by van der Waals forces and electrostatic attractions collect individual particles together to form agglomerates.[30–32] Therefore, we observe that MOF powders are not fluidized as individual particles but largely as porous agglomerates with various size distributions (see Figure 3). The fluidization can be homogenized along the height of the bed chamber using a slightly divergent, diffuser-style vessel geometry,[33] wherein larger (heavier) agglomerates are fluidized closer to the bottom of the bed. Other methods that have been used to assist in the fluidization of cohesive particles include sound excitation, vibration, stirrers, flow pulsation, and mixed particles.[30,34–36]

We observe that agglomerating fluidization results in approximately spherical agglomerates with diameters varying from microscopic to millimeter scale, consistent with the observations of a wide range of other powders.[31,32,37] Consequently, we hypothesize that during fluidization, a portion of airstream flows through the porous agglomerates, as in the classic case of a porous sphere in a flow.[38] For a given flow rate, the water vapor transported in and out of any form of porous adsorbent agglomerates, *a*, can be described by a convection-diffusion equation of the following form[9,10,39,40]:

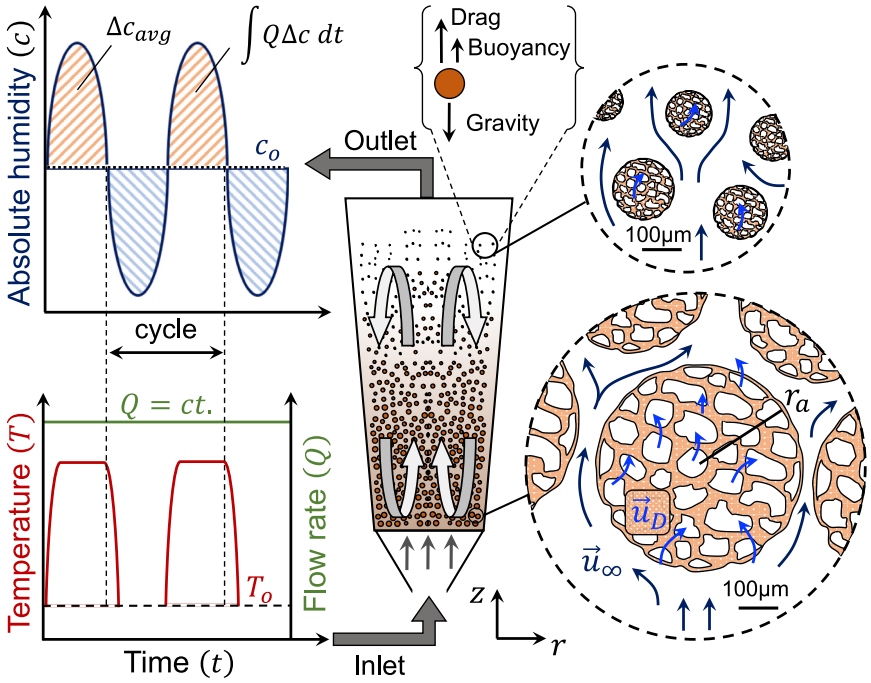

Figure 1. Schematic of a Fluidized Bed Design for the Sorption Component of an Atmospheric Water Harvesting System

The solid particulates consist of adsorbents in fine powder or their granular agglomerates (in this work, metal-organic frameworks, MOFs). The largest particles are spherical porous agglomerates of a few hundred microns in diameter. The very high surface-to-volume ratio enables rapid diffusion dynamics, and hence, high-frequency operation of the adsorbent cell. For a given flow rate, a periodically varied temperature of the input flow drives moisture adsorption and desorption to and from the adsorbent. Continuously cycled water vapor harvesting can be thus achieved at the exit of the fluidized bed, increasing dramatically the amount of water vapor collected per mass of adsorbent per day.

$$\frac{\partial c_w}{\partial t} = \nabla\cdot(D_v\nabla c_w) - \nabla\cdot(\vec{u}_D c_w) + \frac{1-\varepsilon_a}{\varepsilon_a}R_s, \qquad \text{(Equation 1)}$$

where c_w is the water vapor concentration, D_v is the intercrystalline mass diffusivity of agglomerates, $\vec{u}_D$ is the superficial velocity through the voids of agglomerate (Darcy velocity), and R_s is the instantaneous rate of adsorption (or desorption) described by a linear driving force (LDF) model[40,41]:

$$R_s = \frac{15}{r_c^2}D_c\langle c_{w,eq} - c_{w,c}\rangle. \qquad \text{(Equation 2)}$$

Here, D_c and r_c are the mass diffusivity and radius of a single MOF crystal in the aggregate (smallest characteristic length scale), $c_{w,eq}$ is the equilibrium concentration obtained from adsorption isotherms, and $\langle c_{w,c}\rangle$ is the instantaneous water vapor concentration inside the single crystals of the agglomerate. Here, we consider a simple analysis of the transport in this problem based on the previous two equations. For rapid mass transport, there are at least three characteristic time scales that should be kept small to achieve fast response operation of a fluidized adsorbent cell. These include: (1) advective transport along the fluidized bed expansion length H, (2) diffusion over individual adsorbent crystals, and (3) transport (diffusive and advective) within the fluidized porous agglomerates. These characteristic times respectively scale as follows: H/u_∞, r_c^2/D_c, and $\min(r_a^2/D_v, r_a/u_D)$. For the latter, we heuristically consider the minimum time scale of two competing transport

modes within agglomerates of the variable radius r_a. These are discussed further below.

First, the velocities required for fluidization in Earth's gravity are sufficiently high that the transport time scale H/u_∞ is negligibly small. In our setup, this time is ~0.05 s. The second time scale r_c^2/D can be interpreted as the diffusive transport time required to drive water into and out of the characteristic radius r_c of the smallest adsorbent crystal material and is determined by the nature of the adsorbent material itself. This time scale is not influenced by fluidization and, provided that the non-porous grains (or individual crystals) are sufficiently small, represents the optimum theoretical limit to the productivity of the maximizing system. In such a case, the water vapor adsorption and desorption are diffusion limited as per Equation 2. The transport in a fluidized bed is hence most likely limited by the third mode of transport: the coupled advective-diffusion timescale for transport into and out of the largest porous agglomerates, characterized by $\min(r_a^2/D_v, r_a/u_D)$. The latter transport is greatly influenced by both the fluidization air velocity field and the characteristic size of agglomerates formed during the adsorption-desorption phases. For example, we observe small qualitative variations in the diameter of these grains during the cycle (cf. Figure 3). Despite such formations, and as we will demonstrate quantitatively below, we observe that fluidization results in much improved transport rates relative to typical packed bed-type MOF form factors. We attribute this to two reasons. First, the radii of these porous agglomerates are observably a few hundred microns (see Figure 3C), which is significantly smaller than the millimeter order size of the packed bed MOF layers reported in the literature.[9–11,14] Second, the porous agglomerates in our fluidized bed are exposed to a high momentum airstream impinging directly onto the agitated agglomerates. We hypothesize that this results in a significant advective flux term $\nabla\cdot(\vec{u}_D c_w)$ within the air-filled porous of agglomerates. The ratio of advective-to-diffusive transport fluxes within the porous agglomerates can be characterized by scaling the ratio of the first and second terms on the right-hand side of Equation 1 to yield a Péclet number of the form $r_a u_D/D_v$. Our observations of porous agglomerate size and porosity (see below) and the rapid adsorption-desorption response of our system suggest that this Péclet number is greater than unity (see Data S1, Figure S6, and Tables S1–S3).

Lastly, we briefly comment on limitations related to heat transport. In the current design, we drive cycles by varying the input temperature, with a rectangular wave as the approximate model waveform. The time required for heat transfer may also limit the ultimate performance. We hypothesize that the rate of heat transport within the air and MOF material within the fluidized agglomerate bodies is at least comparable to that of mass transport. For example, note that the characteristic Lewis number within the heterogeneous network of intercrystalline voids spaces of agglomerates is significantly higher than unity (see Table S1). Hence, we estimate that a thermal Péclet number of the form $r_a u_D/\alpha_v$ is also greater than unity. This is consistent with our earlier hypotheses of mass transfer and suggests a significant contribution of the advective flux term on the heat transfer process. This suggests that the thermal response time scale of our current system is limited by the temperature cycling of the test structure itself (via forced thermal convection). The thermal mass of the solid structure includes the diffuser-shaped bed chamber, the flow fittings, and the inlet tubing of the device. We estimate this thermal mass to be on the order of 1 kJ/K. We plan to study this coupling between thermal transport and mass transport and adsorption-desorption in future work.

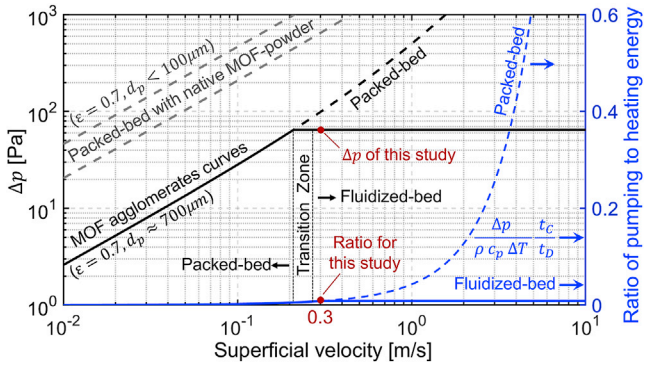

Figure 2. Comparison of Pumping and Heating Energy Requirements for Fluidized MOF

(Left axis) Pressure drop versus superficial velocity diagram for packed and fluidized bed arrangements of the geometry of our system ($L \sim 15$ mm, $D = 15$ mm). The pressure drop is a prediction based on Ergun's equation,[42] considering the thermophysical properties of MOF-801, a particle sphericity of 0.95, and a bed porosity of 0.7. (Right axis) Pumping energy to drive the air through the fluidized bed normalized by the heating energy requirements for regeneration. Here, we consider a temperature increase of 40°C compared to ambient conditions and a desorption phase duration of 25% of the cycle ($t_D t_C^{-1} = 0.25$). The hydraulic energy demands are only a small fraction of the energy required for MOF-801 regeneration, either in a packed or a fluidized bed configuration. Therefore, we chose to fluidize the MOF-801 agglomerates to ensure high mass and heat transfer rates while maintaining the pumping energy demands at levels similar to packed bed arrangements.

Hydraulic Power Is Negligible Compared to Heating Power

The energy input into sorption-based systems of the type discussed here are heating of air, which is necessary for regeneration, and the energy required to pump air through the system. Ignoring any losses in supply lines, these are respectively $\dot{m}c_p\Delta T$ and $Q\Delta p$, where $\dot{m}c_p$ is the thermal mass of the airstream, ΔT the temperature rise, Q the volumetric flow rate, and Δp the pressure drop across the adsorbent bed. In Figure 2, we used Ergun's correlation[42] to predict Δp for MOF-801 packed bed columns of the length of our fluidized bed ($L \sim 15$ mm), and we plot the pressure loss versus the superficial air velocity through the bed. As a relevant comparison, we show pressure drop curves for a packed bed configuration of the native powder form and for the MOF agglomerates generated after running a fluidized bed. As for the latter, the transition zone for the MOF agglomerates was estimated experimentally by gradually increasing the flow rate until complete fluidization at ~0.3 m/s. Above this transition zone, Δp remains approximately constant and a further increase in superficial velocity results in fluidized bed expansion, eventually resulting in the so-called pneumatic transport regime (not shown here). In contrast to this fluidized bed situation, packing of the MOFs in their native powder form typically produces porous solid form factors with particle diameters <100 μm.[15–20] For such packed beds, we estimate a permeability of 2.3E−10 m^2, and this results in a significant pressure drop for a given superficial velocity, as shown in the left axis of Figure 2. Together with the pressure drop information, the right ordinate of the plot shows the ratio of pumping-to-heating energy requirements, considering that the desorption phase is 25% of the cycle duration. For superficial velocities <1 m/s, the pumping energy is only a small fraction of the heating requirements and ~1% in the case of a fluidized bed. Consequently, we chose to fluidize just above the minimum fluidization velocity to achieve high mass and heat transport rates, and hence high-frequency operation, while maintaining a negligible (compared to heating) air pumping power.

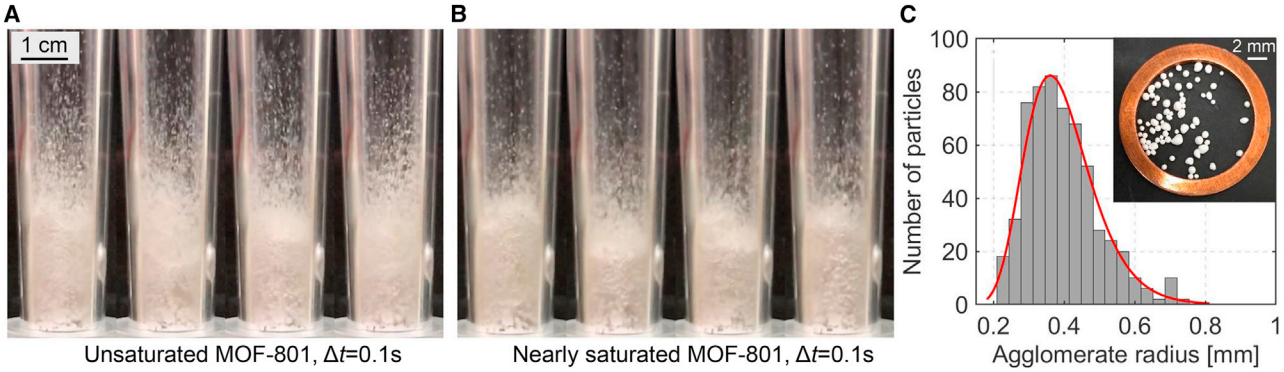

Figure 3. Illustration of MOF-801 Fluidization and Agglomerate Characterization

(A and B) Instantaneous images of fluidized MOF-801 powder during the adsorption process at (A) unsaturated and (B) nearly saturated conditions show a bubbling fluidization behavior over the full length of bed expansion and spherical agglomerates of various size distribution. The images shown were taken at time intervals of 0.1 s and exemplify fast particle motion and vigorous stirring within the fluidized bed. In the splashing zone, small grains are ejected upward at distances up to three times the fluidized bed height, while larger agglomerates are fluidized closer to the bottom of the bed.

(C) The radius of MOF-801 agglomerates show a log-normal distribution with a mean value of 395 μm. Assuming a spherical profile, the cumulative volume of ~600 particles (128 mg weight) revealed an average agglomerate porosity of 72%.

Observed Fluidization Dynamics and Quantification of Agglomerate Distribution

Figures 3A and 3B show representative images during the adsorption process of MOF-801. At the top of the fluidized bed, the splashing zone is characterized by smooth fluidization wherein very small grains are ejected upward, creating a fountain of flowing particles, schematically indicated in Figure 1. Fluidization velocities are lower near the walls of the vessel; thus, particles fall visibly convect downward near the walls. These mix with the bottom portion of the bed surface and the process is repeated. Note that the main core of the bed exhibits a bubbling fluidization behavior, which is a necessary condition for appropriate mixing dynamics.[43,44] The images also show individual spherical agglomerates with radii ranging from a maximum of ~0.5 mm down to on the order of microns. Analysis of correlated image sequences also shows particles distributed throughout the length of the bed, with the largest particles in locations near the inlet (bottom) of the bed. Preliminary experiments (not shown here) with a bed chamber of approximately the same length but with constant diameter exhibited a very bimodal adsorbent location distribution, with many small particles "packed" into the top filter and many larger particles near the inlet (and many of these hardly fluidized). We attribute the broad placement distribution and strong agitation of the current system to the divergent, diffuser-like shape of the bed chamber, which has been shown to favor such fluidization dynamics.[33] We also noticed that the agglomerates are the smallest and more actively fluidized (e.g., to higher heights) near the beginning of the adsorption process. Near the end of adsorption, by contrast, there is a noticeable shift of particles toward the bottom of the bed. The latter is consistent with both larger agglomerates and higher-density material associated with water adsorption. Adsorption and desorption videos of the fluidized MOF-801 powder are provided as Video S1, including instantaneous images over the cycle (see Data S1 and Figure S5).

We performed some simple image analyses of the MOF-801 material after several fluidization cycles. To this end, we extracted a collection of particles biased in favor of the largest particles (by gently pouring out part of the material onto a small collection plate). We were particularly interested in these largest agglomerates as they likely limit the maximum rate of air-to-particle center transport of water vapor. We

collected ~600 of these larger spherical particles and obtained 6 images like the example shown in Figure 3C. We developed a custom image analysis tool in MATLAB (using standard thresholding and morphological image processing) and used this to quantify the radius of these large agglomerates. Figure 3C shows that the radius of these largest collected agglomerates varied between 200 and 650 μm, with a mean radius of 395 μm. This diffusion length scale is an order of magnitude smaller than the characteristic thicknesses of 2.57 mm,[9] 2.54 mm,[10] and 3 mm[14] for packed bed MOF layers used in prior studies. After quantifying their size distribution, we weighed these largest grains in a mass balance and combined this with the size distribution to estimate an average porosity of ~0.72. This value is very close to the reported optimum porosity 0.7 for the maximum yield of atmospheric water harvesting cycle materials.[8] The aforementioned data support the hypotheses and scaling arguments presented earlier and described schematically in Figure 1. The porosity, degree of agitation (and levitation) of such particles, and the fast response of the system (see below) also support the hypothesis that the advective flux term in Equation 1 is important for the interparticle moisture transport.

Measurements Showing High-Frequency Water Vapor Harvesting

High-frequency adsorption-desorption operation of the fluidized MOF-801 material was obtained at 18% and 39% RH, for at least 10 consecutive cycles. The first cycle shows different behavior due to initial transients in both temperature and MOF water content and to slight adjustments of flow conditions that occur only during that first cycle. The system thereafter quickly reaches a dynamic steady state. The criterion to end each adsorption and begin each desorption phase (and vice versa) was chosen as the instance when the inlet-to-outlet absolute humidity difference was <5%.

Figure 4A shows the variation of inlet temperatures, which, for both experiments, have shape characteristics consistent with the first-order thermal response of the system (upon forcing with the rectangular wave input associated with the inlet valve operation). During desorption, the temperature first increases rapidly and the slope begins to decrease, reaching ~75°C and >80°C at the end of the phase for RH values of 18% and 39%, respectively. For the adsorption phase, the temperature falls rapidly and then begins to level off, reaching the inlet ambient conditions. These temperature differences are sufficient to drive adsorption and desorption as per well-characterized adsorption isotherms of MOF-801[9–11,45] (see Figure 5C). The outcome of this cyclic temperature variation is directly reflected on the water vapor content at the exit of the fluidized bed, shown in Figure 4B. For the desorption phase at 18% and 39% RH, the outlet absolute humidity increases rapidly to maximum values of ~8 and 13 g/m^3, respectively, as water is released from the bed. For the adsorption phase, the outlet absolute humidity decreases, achieves a minimum, and then begins to increase gradually toward the inlet conditions and as the MOF-801 becomes saturated. Note the complex shapes of the humidity cycle curves and the qualitative difference in shape between the two RH values. We hypothesize that these shapes are influenced by RH levels and the gradient of the sigmoidal adsorption isotherms (cf. Figure 5C), the aforementioned dynamic changes in size distribution of aggregates, the unsteady heat transfer in the system, and the complex fluid flow within the fluidized bed (among other factors). We plan to characterize and study these complex dynamics as part of our future work.

Figures 4C and 4D summarize the cycle-to-cycle repeatability of the complex shape of the humidity curves for our experiment. Plotted are direct overlays of cycles 2–10. We see excellent quantitative agreement in the shape and magnitude of consecutive

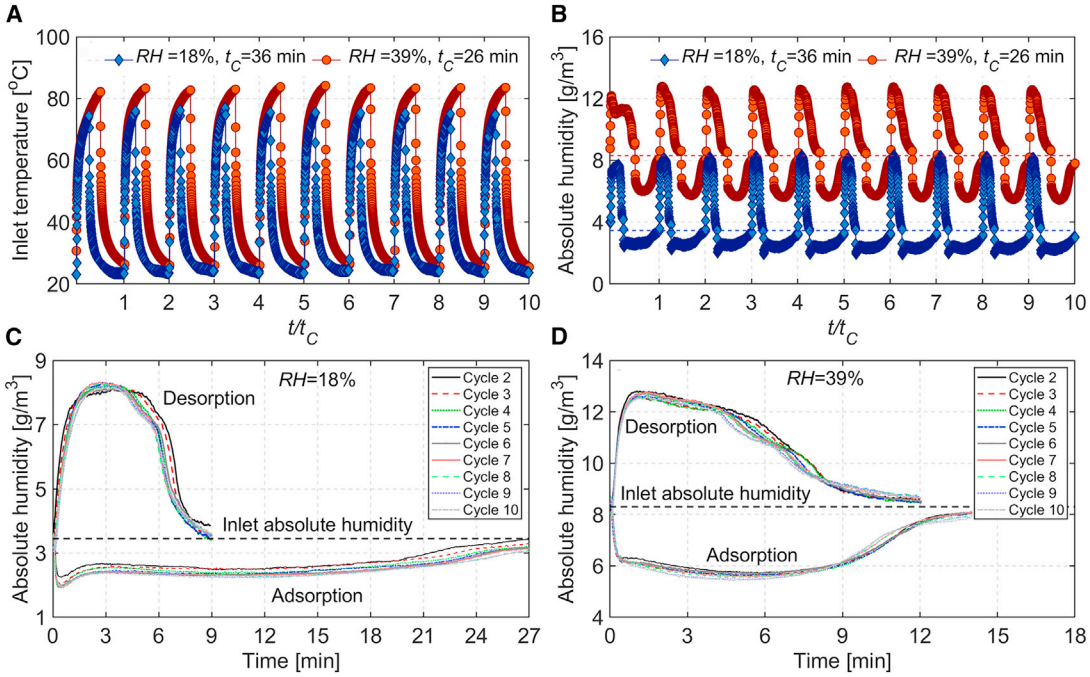

Figure 4. Dynamic Steady-State and Continuous Cyclic Sorption Dynamics

High-frequency operation of MOF-801 in a fluidized bed for 18% and 39% RH and 10 consecutive cycles.

(A) Variation of inlet temperature that drives adsorption and desorption dynamics.

(B) Water vapor content at the exit of the fluidized bed indicates dynamic steady-state conditions even from the adsorption process of the first cycle. Furthermore, no degradation in terms of water vapor capacity was observed, indicating the recyclability of the process.

(C and D) Temporal evolution of water vapor content at the exit of the fluidized bed for (C) 18% and (D) 39% RH indicates the repeatability between individual cycles and the fast response operation of the adsorbent cell. The adsorption-desorption vapor harvesting cycle can be achieved within only 36 and 26 min at 18% and 39% RH. This demonstrates the potential of 40 and 55 cycles per day to dramatically increase the throughput of the system per mass of MOF-801 per day.

cycles. We attribute this to the reproducible dynamics of fluidization, including bubbling dynamics of the lower bed contents. This repeatability is also strong evidence of the negligible degradation of sorbent capacity—at least for the operating times considered here (more than on the order of 100 h of operation). Here, the water vapor content is plotted as a function of time to demonstrate the fast response operation of the fluidized adsorbent cell. At 18% RH, desorption and adsorption phases last 9 and 27 min, respectively (see Figure 4C). A complete cycle duration is thus only 36 min, which in turn results in 40 cycles per day. Similarly, at 39% RH, desorption and adsorption are completed within 12 and 14 min, respectively (see Figure 4D). This constitutes an adsorption-desorption cycle in 26 min and thus the potential for >55 cycles per day. The water uptake process is, as expected, slower for 18% RH (27 min) compared to 39% RH (14 min). As we discuss below (see Equation 4), the important figure of merit for productivity capacity is the product of per-cycle mass capacity of the adsorbent and the number of cycles per day.

The demonstrated high-frequency operation associated with MOF-801 fluidization can be further appreciated by comparing these results to published data using a 3-mm-thick packed bed geometry of MOF-303 and a parallel convective flow normal for this thickness.[14] The latter system was operated for 450 min at 22% RH, and this duration of adsorption was insufficient to saturate the material. At 39% RH, the system was reportedly saturated after an adsorption phase of ~300 min. By comparison, the current fluidization of MOF-801 results in an adsorption phase with a time

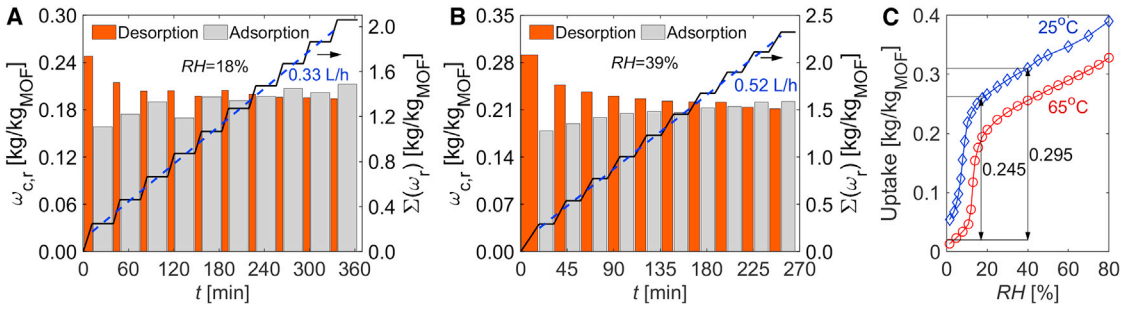

Figure 5. Water Vapor Captured and Released per Cycle during Fluidization of MOF-801

(A and B) Measurements of the amount of water vapor content captured and released per cycle during fluidization of MOF-801 at (A) 18% and (B) 39% RH. The second ordinate on the right and black curve are based on integrations of the measured humidity during desorption and indicate the cumulative water that was removed.

(C) Based on adsorption isotherms , these data imply a continuous cyclic operation at >75% of MOF-801 available uptake capacity, and hence, very high moisture harvesting rates of 0.33 and 0.52 L/kg_{MOF}/h. The data for the adsorption isotherms were obtained from Kim et al.[9]

scale that is 20 to 25 times faster for similar RH values. These data demonstrate the possibility of achieving exceptionally high operating frequencies using MOFs in their native particulate form within a fluidized bed.

The performance of a sorption-based atmospheric water harvester greatly depends on the total mass of water captured and released normalized by the sorbent mass. For given volumetric flow rate, Q, the water mass captured (ω_w^c) and mass released (ω_w^r) can be estimated as follows:

$$\omega_w^{c,r} = \frac{Q}{m_{MOF}} M \int \Delta c dt. \qquad \text{(Equation 3)}$$

Here, Δc is the instantaneous difference of water vapor molar density between inlet and outlet conditions, Δt is the time duration of adsorption or desorption, M is the molecular weight of water, and m_{MOF} the mass of MOF-801. Figure 5 shows that the amount of captured and released water vapor per cycle is constant as the system adopts dynamic steady state conditions. In particular, an average of 0.198 and 0.223 kg of water vapor per kilogram of MOF-801 can be harvested per cycle, at 18% and 39% *RH*, respectively. These measured values are very close to the respective measured maximum overall uptake capacity of MOF-801 which is about 0.26 (18% *RH*) and 0.31 (18% *RH*) kg/kg_{MOF}[9–11] (cf. Figure 5C). Note also that the desorption explored here was performed using relatively moderate temperature differences. These temperatures imply that MOF-801 cannot be re-generated completely, resulting in retained water vapor of ~0.015 kg/kg_{MOF}. Hence, the current working capacities of 0.245 and 0.295 kg/kg_{MOF}, as indicated in Figure 5C, are ~80% and 76% of the available uptake capacity at 18% and 39% RH. We can also define a system water vapor productivity P as the mass of moisture recovered per time and per mass of adsorbent (L/kg_{MOF}/day) for many cycles as follows:

$$P = f\omega_w^r \kappa. \qquad \text{(Equation 4)}$$

Here, f is the frequency of the cyclic operation (cycles per day) and κ is the fraction of time during the day when the system is operated. For κ values of approximately unity, the water vapor harvesting rates of our system are estimated as 0.33 and 0.52 L/h per kilogram of MOF-801 for RH values of 18% and 39%, respectively (see Figure 5). We attribute such high values of water vapor productivity to the rapid cyclic periods of 36 min (18% RH) and 26 min (39% RH) obtained with fluidization.

DISCUSSION

Various figures of merit have been used and proposed to quantify the performance of AWH technologies.[46,47] Perhaps the most important of these is the amount of water produced normalized by the mass of adsorbent material. For this figure of merit, high-frequency sorption dynamics is essential, and the MOF material form factor should be optimized not only for small characteristic length scales appropriate for rapid mass and heat transport (e.g., porosity, MOF weight per area) but also for leveraging the advection in mass transport, as per the advective flux term of Equation 1. Here, we experimentally demonstrated that the fluidization of MOFs is very promising for achieving exceptionally high operational frequencies leveraging 80% of the uptake capacity of the sorbent. A second figure of merit is the power cost per unit volume of produced water. A preliminary energy assessment of our fluidized adsorbent cell suggests that the energy required to pump the air through the bed is <1% of the heating requirements for regeneration (even at moderate regeneration temperatures) and significantly smaller than the hydraulic power required for packed beds of the native MOF powder. This leads us to consider designs that use low-grade waste heat for regeneration to maximize overall efficiency (e.g., power plant exhaust streams with temperatures on the order of 100°C–120°C. A second possibility is the solar thermal heating of air.[9–11] Note that such uses of waste heat are not easily leveraged for refrigeration-based AWH systems. For refrigeration, input power is typically dominated by electric power applied to a compressor. Furthermore, we hypothesize that dew condensation at energetically favorable temperatures (and perhaps even ambient temperatures) may be achievable by lowering the air flow rate during the desorption phase. This would, of course, come with a penalty of lower overall cycle frequency, and we hope to explore such trade-offs in the future.

We note that a third figure of merit that may influence the design of distributed systems, infrastructure cost, and portability (e.g., in a truck bed) may be the water volume produced per time and per volume of the system (with units of inverse time). For the current system, assuming 70% is recoverable in a condenser, we estimate values of 0.4/s (18% RH) and 0.63/s (39% RH) for our system. Note that we do not include here a figure of merit based on the amount of water yielded versus amount input into the system (e.g., as in a recovery ratio percentage yield of input water) for two reasons. First, unlike desalination or contamination removal technologies, the current system has no cost associated with the "disposal" of processed air. Second, pumping excess air into the system is only important if hydraulic power contributes significantly to operating costs, which we believe is not important relative to other costs of a realistic water harvesting system such as the initial cost of the plant and MOF material, and any operational costs of a downstream condenser.

In summary, we experimentally demonstrated the ability to perform 40 and 55 water vapor adsorption and desorption cycles per day at 18% and 39% RH by fluidizing MOF-801 in its native particulate form. The fluidized bed operation also resulted in the leveraging of ~80% of the MOF-801 maximum uptake capacity with cyclic periods of 36 min (18% RH) and 26 min (36% RH). The moisture harvesting rates of our system are estimated at 0.33 L/h (18% RH) and 0.52 L/h (39% RH) per kilogram of MOF-801, and this is at least an order of magnitude higher than the existing methods incorporating packed bed MOF shape bodies. Therefore, this fluidized MOF adsorbent approach has the potential to significantly improve the sorption unit of an atmospheric water harvester with a scalable and high flow capacity form

factor. Plausible extensions of the current work include the optimization of the fluidization process for large-scale energy engineering applications, including CO_2 capturing, as well as the development of heat and mass transport models to simulate the complex dynamics of fluidized atmospheric water harvesters under various meteorological conditions.

EXPERIMENTAL PROCEDURES

Experimental Remarks

All water vapor sorption cycling experiments were conducted at a newly designed test facility described in Data S1 (see Figures S1–S3). The system has an operational principle depicted in the schematic of Figure 1. The solid particulates in the fluidized bed consist of ~0.52 g activated MOF-801 in its native particulate form. Scanning electron microscopy (SEM) images of the powdered MOF-801 (see Data S1 and Figure S4) revealed an average crystal diameter of 0.4 μm. The system is able to pre-treat and generate dry-air and water-vapor airflow mixtures with an accuracy of 1% in the range of 0%–70% RH. The temperature of the air-vapor mixture can also be set independently of absolute humidity by diverting all or part of the airflow through a heat exchanger powered by an electric heater. The system can valve between cold (adsorption) and hot (desorption) flow input streams using a three-way valve. The temporal dynamics of the RH and temperature upstream and downstream of the fluidized bed are measured with two humidity-temperature sensors (Sensirion SEK-SHT35). During data acquisition, the absolute humidity and the dew point of the measurement locations are concurrently calculated with the Arden Buck equation for the water vapor saturation pressure.[48] We evaluated system performance at several inlet conditions and chose the following two inlet boundary conditions: 18% RH at 22°C and 39% RH at 23.5°C. The system first achieved appropriate inlet conditions, and then, the flow rate was gradually increased until complete fluidization with full bed expansion was obtained. For a bed height of ~15 mm, this resulted in a fluidization velocity of 0.3 m/s. Note that this value is very close to empirical correlations applicable for uniform particle sizes (e.g., Wen and Yu equation).[49] If we consider as a characteristic particle scale the largest grain diameter, ~1 mm (see Figure 3C), these relations yield a fluidization velocity in the range of 0.2–0.5 m/s, depending on particle sphericity and porosity of the (initially) packed bed. The volumetric flow associated with the current fluidization velocity (0.3 m/s) was ~6E−5 m^3/s. The temporal saturation condition of MOF-801 is controlled by comparing the absolute humidity level before and after the fluidized bed. As soon as the MOF-801 solid particulates are saturated (i.e., absolute humidity differences are within experimental uncertainties), the inlet temperature is periodically varied to initiate the adsorption and desorption dynamics of the fluidized adsorbent cell for 10 consecutive operational cycles.

DATA AND CODE AVAILABILITY

All of the data are available from the Lead Contact upon reasonable request.

SUPPLEMENTAL INFORMATION

Supplemental Information can be found online at https://doi.org/10.1016/j.xcrp.2020.100057.

ACKNOWLEDGMENTS

The authors acknowledge the TomKat Center for Sustainable Energy, Stanford University for the funding support. The authors are also grateful to Dr. Kang Liu from

Wuhan University (China) for supplying the MOF-801 powder, as well as to Prof. Yi Cui from the Department of Materials Science and Engineering at Stanford University for his overall contribution.

AUTHOR CONTRIBUTIONS

Conceptualization, J.G.S.; Design, A.T. and J.G.S.; Experimentation, Post-processing, & Data Analysis, A.T.; Writing, A.T. and J.G.S.; Review & Editing, A.T., A.R., K.W., M.A., K.E.G., and J.G.S.; Funding Acquisition, J.G.S. and K.E.G.

DECLARATION OF INTERESTS

The authors declare no competing interests.

Received: January 30, 2020
Revised: March 13, 2020
Accepted: March 26, 2020
Published: May 20, 2020

REFERENCES

1. Shiklomanov, I. (1993). World fresh water resources. In Water in Crisis: A Guide to the World's Fresh Water Resources, *Chapter 2*, P.H. Gleick, ed. Water in Crisis: A Guide to the World's Fresh Water Resources (Oxford University Press).
2. Alayli, Y., Hadji, N.E., and Leblond, J. (1987). A new process for the extraction of water from air. Desalination *67*, 227–229.
3. Li, H., Eddaoudi, M., O'Keeffe, M., and Yaghi, O.M. (1999). Design and synthesis of an exceptionally stable and highly porous metal-organic framework. Nature *402*, 276–279.
4. Yaghi, O.M., O'Keeffe, M., Ockwig, N.W., Chae, H.K., Eddaoudi, M., and Kim, J. (2003). Reticular synthesis and the design of new materials. Nature *423*, 705–714.
5. Furukawa, H., Gándara, F., Zhang, Y.-B., Jiang, J., Queen, W.L., Hudson, M.R., and Yaghi, O.M. (2014). Water adsorption in porous metal-organic frameworks and related materials. J. Am. Chem. Soc. *136*, 4369–4381.
6. Kalmutzki, M.J., Diercks, C.S., and Yaghi, O.M. (2018). Metal-Organic Frameworks for Water Harvesting from Air. Adv. Mater. *30*, e1704304.
7. Canivet, J., Fateeva, A., Guo, Y., Coasne, B., and Farrusseng, D. (2014). Water adsorption in MOFs: fundamentals and applications. Chem. Soc. Rev. *43*, 5594–5617.
8. LaPotin, A., Kim, H., Rao, S.R., and Wang, E.N. (2019). Adsorption-Based Atmospheric Water Harvesting: Impact of Material and Component Properties on System-Level Performance. Acc. Chem. Res. *52*, 1588–1597.
9. Kim, H., Yang, S., Rao, S.R., Narayanan, S., Kapustin, E.A., Furukawa, H., Umans, A.S., Yaghi, O.M., and Wang, E.N. (2017). Water harvesting from air with metal-organic frameworks powered by natural sunlight. Science *356*, 430–434.
10. Kim, H., Rao, S.R., Kapustin, E.A., Zhao, L., Yang, S., Yaghi, O.M., and Wang, E.N. (2018). Adsorption-based atmospheric water harvesting device for arid climates. Nat. Commun. *9*, 1191.
11. Fathieh, F., Kalmutzki, M.J., Kapustin, E.A., Waller, P.J., Yang, J., and Yaghi, O.M. (2018). Practical water production from desert air. Sci. Adv. *4*, eaat3198.
12. Rieth, A.J., Yang, S., Wang, E.N., and Dincă, M. (2017). Record Atmospheric Fresh Water Capture and Heat Transfer with a Material Operating at the Water Uptake Reversibility Limit. ACS Cent. Sci. *3*, 668–672.
13. Rieth, A.J., Wright, A.M., Skorupskii, G., Mancuso, J.L., Hendon, C.H., and Dincă, M. (2019). Record-Setting Sorbents for Reversible Water Uptake by Systematic Anion Exchanges in Metal-Organic Frameworks. J. Am. Chem. Soc. *141*, 13858–13866.
14. Hanikel, N., Prévot, M.S., Fathieh, F., Kapustin, E.A., Lyu, H., Wang, H., Diercks, N.J., Glover, T.G., and Yaghi, O.M. (2019). Rapid Cycling and Exceptional Yield in a Metal-Organic Framework Water Harvester. ACS Cent. Sci. *5*, 1699–1706.
15. Howarth, A.J., Liu, Y., Li, P., Li, Z., Wang, T.C., Hupp, J.T., and Farha, O.K. (2016). Chemical, thermal and mechanical stabilities of metal–organic frameworks. Nat. Rev. Mater. *1*, 15018.
16. Carné-Sánchez, A., Imaz, I., Cano-Sarabia, M., and Maspoch, D. (2013). A spray-drying strategy for synthesis of nanoscale metal-organic frameworks and their assembly into hollow superstructures. Nat. Chem. *5*, 203–211.
17. Chen, Y., Zhang, S., Cao, S., Li, S., Chen, F., Yuan, S., Xu, C., Zhou, J., Feng, X., Ma, X., and Wang, B. (2017). Roll-to-Roll Production of Metal-Organic Framework Coatings for Particulate Matter Removal. Adv. Mater. *29*, 1606221.
18. Majchrzak-Kucęba, I., and Ściubidło, A. (2019). Shaping metal–organic framework (MOF) powder materials for CO_2 capture applications - a thermogravimetric study. J. Therm. Anal. Calorim. *45*, 1–6.
19. Valekar, A.H., Cho, K.-H., Lee, U.-H., Lee, J.S., Yoon, J.W., Hwang, Y.K., et al. (2017). Shaping of porous metal–organic framework granules using mesoporous ρ-alumina as a binder. RSC Advances *7*, 55767–55777.
20. Yuan, S., Feng, L., Wang, K., Pang, J., Bosch, M., Lollar, C., Sun, Y., Qin, J., Yang, X., Zhang, P., et al. (2018). Stable Metal-Organic Frameworks: Design, Synthesis, and Applications. Adv. Mater. *30*, e1704303.
21. Burtch, N.C., Heinen, J., Bennett, T.D., Dubbeldam, D., and Allendorf, M.D. (2018). Mechanical Properties in Metal-Organic Frameworks: Emerging Opportunities and Challenges for Device Functionality and Technological Applications. Adv. Mater. *30*, e1704124.
22. Rüdisüli, M., Schildhauer, T.J., Biollaz, S.M.A., and van Ommen, J.R. (2012). Scale-up of bubbling fluidized bed reactors — a review. Powder Technol. *217*, 21–38.
23. Jiménez-García, G., Aguilar-López, R., and Maya-Yescas, R. (2011). The fluidized-bed catalytic cracking unit building its future environment. Fuel *90*, 3531–3541.
24. Stark, A.K., Altantzis, C., Bates, R.B., and Ghoniem, A.F. (2016). Towards an advanced reactor network modelling framework for fluidized bed biomass gasification: incorporating information from detailed CFD simulations. Chem. Eng. J. *303*, 409–424.
25. Luz, I., Soukri, M., and Lail, M. (2018). Flying MOFs: polyamine-containing fluidized MOF/SiO_2 hybrid materials for CO_2 capture from post-combustion flue gas. Chem. Sci. (Camb.) *9*, 4589–4599.
26. Raganati, F., Ammendola, P., and Chirone, R. (2014). CO_2 capture performances of fine solid sorbents in a sound-assisted fluidized bed. Powder Technol. *268*, 347–356.
27. Wang, Q., Gao, X., Xu, J.Y., Maiga, A.S., and Chen, G.M. (2012). Experimental investigation on a fluidized-bed adsorber/desorber for the

adsorption refrigeration system. Int. J. Refrig. *35*, 694–700.

28. Chen, C.-H., Schmid, G., Chan, C.-T., Chiang, Y.-C., and Chen, S.-L. (2015). Application of silica gel fluidised bed for air-conditioning systems. Appl. Therm. Eng. *89*, 229–238.

29. Geldart, D. (1973). Types of gas fluidization. Powder Technol. *7*, 285–292.

30. Seville, J.P.K., Willett, C.D., and Knight, P.C. (2000). Interparticle forces in fluidization: a review. Powder Technol. *113*, 261–268.

31. Geldart, D., Harnby, N., and Wong, A.C. (1984). Fluidization of cohesive powders. Powder Technol. *37*, 25–37.

32. van Ommen, J.R., Valverde, J.M., and Pfeffer, R. (2012). Fluidization of nanopowders: a review. J. Nanopart. Res. *14*, 737.

33. Gernon, T.M., and Gilbertson, M.A. (2012). Segregation of particles in a tapered fluidized bed. Powder Technol. *231*, 88–101.

34. Ali, S.S., Basu, A., Alfadul, S.M., and Asif, M. (2019). Nanopowder Fluidization Using the Combined Assisted Fluidization Techniques of Particle Mixing and Flow Pulsation. Appl. Sci. (Basel) *9*, 572.

35. Valverde, J.M., Castellanos, A., and Quintanilla, M.A.S. (2001). Effect of vibration on the stability of a gas-fluidized bed of fine powder. Phys. Rev. E Stat. Nonlin. Soft Matter Phys. *64*, 021302.

36. Zhu, C., Liu, G., Yu, Q., Pfeffer, R., Dave, R.N., and Nam, C.H. (2004). Sound assisted fluidization of nanoparticle agglomerates. Powder Technol. *141*, 119–123.

37. Turchiuli, C., Eloualia, Z., El Mansouri, N., and Dumoulin, E. (2005). Fluidized bed agglomeration: Agglomerates shape and end-use properties. Powder Technol. *157*, 168–175.

38. Srivastava, A.C., and Srivastava, N. (2005). Flow past a porous sphere at small Reynolds number. Z. Angew. Math. Phys. *56*, 821–835.

39. Narayanan, S., Yang, S., Kim, H., and Wang, E.N. (2014). Optimization of adsorption processes for climate control and thermal energy storage. Int. J. Heat Mass Transfer *77*, 288–300.

40. Hefti, M., and Mazzotti, M. (2014). Modeling water vapor adsorption/desorption cycles. Adsorption *20*, 359–371.

41. Sircar, S., and Hufton, J.R. (2000). Why Does the Linear Driving Force Model for Adsorption Kinetics Work? Adsorption *6*, 137–147.

42. Ergun, S. (1952). Fluid flow through packed columns. Chem. Eng. Prog. *48*, 89–94.

43. Bakshi, A., Altantzis, C., Glicksman, L.R., and Ghoniem, A.F. (2017). Gas-flow distribution in bubbling fluidized beds: CFD-based analysis and impact of operating conditions. Powder Technol. *316*, 500–511.

44. Bakshi, A., Ghoniem, A.F., and Altantzis, C. (2017). Mixing dynamics in bubbling fluidized beds. AIChE J. *63*, 4316–4328.

45. Burhan, M., Shahzad, M.W., and Ng, K.C. (2019). A Universal Theoretical Framework in Material Characterization for Tailored Porous Surface Design. Sci. Rep. *9*, 8773.

46. Tu, Y., Wang, R., Zhang, Y., and Wang, J. (2018). Progress and Expectation of Atmospheric Water Harvesting. Joule *2*, 1452–1475.

47. Bagheri, F. (2018). Performance investigation of atmospheric water harvesting systems. Water Resour. Ind. *20*, 23–28.

48. Buck, A.L. (1981). New Equations for Computing Vapor Pressure and Enhancement Factor. J. Appl. Meteorol. *20*, 1527–1532.

49. Wen, C.Y., and Yu, Y.H. (1966). A generalized method for predicting the minimum fluidization velocity. AIChE J. *12*, 610–612.

Cell Reports Physical Science, Volume *1*

Supplemental Information

High-Frequency Water Vapor Sorption Cycling Using Fluidization of Metal-Organic Frameworks

Alexandros Terzis, Ashwin Ramachandran, Kecheng Wang, Mehdi Asheghi, Kenneth E. Goodson, and Juan G. Santiago

Supplemental Experimental Procedures

Section 1: Experimental setup and design

A schematic of the experimental test rig is shown in Figure S1. Compressed air is initially filtered and de-humidified in a five-stage desiccant air-drying system (ATD Tools 7888). The desiccant dryer (1) is capable of reducing dew point below –30°C for ambient temperatures (20-25°C) with the use of 3.8 L silica gel beads. At this point, the dried air has a relative humidity below 1%. A portion of this air stream is diverted using valves (2) through a humidification unit. This unit is a small metal chamber that holds a pool of approximately 0.8 L of water with a free surface area of 265 cm^2 over which the air flows (3). The two air streams (dried versus humidified) are then mixed in a Venturi educator mixer (4). This mixer is an ejector (jet pump) design that is also used for humidification purposes.[1] The total flow rate is thereafter measured using an Alicat Scientific MC-5SLPM-D massflow controller (5). At this point, a three-way valve (6) directs the airflow through either a cold (adsorption) or hot (desorption) flow path. For the latter, the temperature of the flow is regulated by four DC-powered electrically heated Clayborn hot-tubes (7). Eventually, both air streams (adsorption or desorption flow path) terminate at the entrance of a cylindrical acrylic vessel used as the fluidized bed (8). This vessel has a diffuser-like shape with a circular cross section and was custom fabricated. The vessel is placed vertically and filled with the metal-organic-framework, MOF-801, in its native particulate form to yield a fluidized bed arrangement for the sorbent material.

The geometrical characteristics of the fluidized bed and the associated instrumentation are shown in Figure S2. Fluidized bed inlet and outlet consist of cylindrical cross section with bottom- and top-diameters of 16 mm and 23 mm, respectively, while the available fluidization length is 90 mm and yields a divergent angle of about 2.2°. The use of a divergent geometry assists to separate particles along the bed height wherein larger (heavier) particles are fluidized closer to the bottom of the bed. This divergent geometry has significant effect on fluidization uniformity.[2] In order to eliminate particulate loss and ensure appropriate airflow distribution in the bed, two stainless steel woven meshes of 53 µm wire diameter and 34% open area were installed upstream and downstream of the fluidized bed, as depicted in Figure S2. The estimation of the air pressure drop through the woven metal meshes is estimated based on literature correlations.[3] For an airstream velocity of 0.3 m/s and the woven mesh characteristics this resulted a pressure drop of about 150 Pa. The upstream filter plays the role of the airflow distributor and such designs have been shown to provide strong mixing dynamics.[4] An additional advantage of the metallic filter is the low thermal resistance (λ/k), where λ and k are the thickness and thermal conductivity of the mesh. In our design, this is estimated 3E-6 $\mathrm{m}^2/(\mathrm{WK})$. This is particularly important during the desorption phase and the rapid heat transport required for the MOF-801 regeneration. Before and after the filters, the temperature and relative humidity

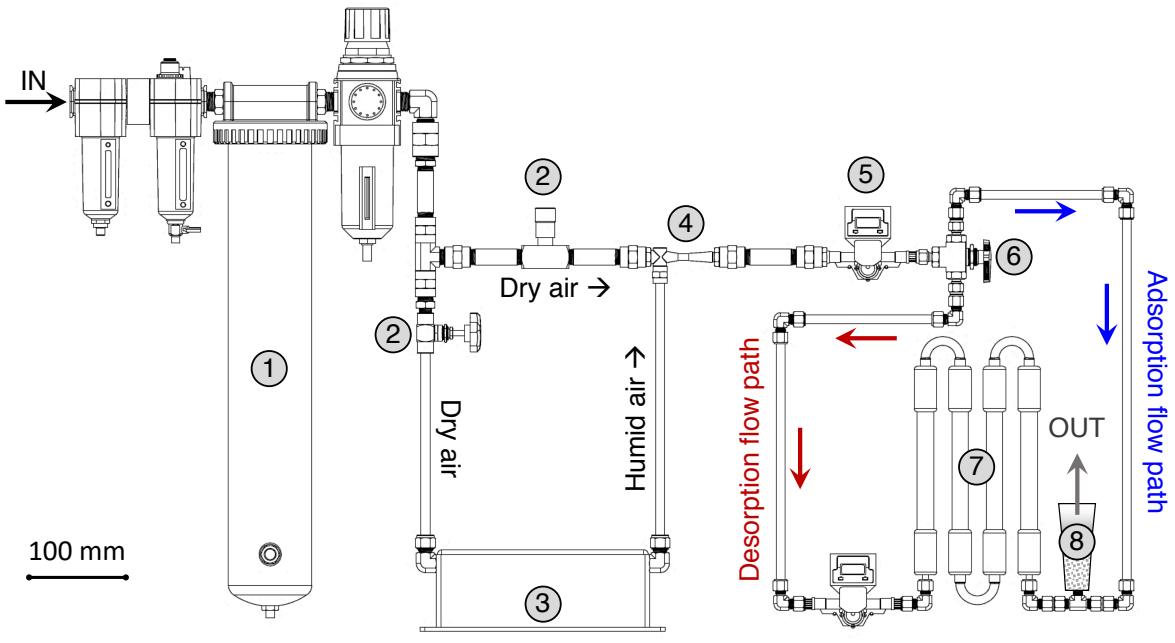

Figure S1. Schematic of experimental test rig used for high-frequency water vapor sorption cycling experiments
The system first dries out all incoming air and then splits this stream into a humidified and dry air streams which can be mixed to achieve desired absolute humidity. The air stream can then be passed through cold (adsorption) or heated (desorption) branches to air conditions input into fluidized bed.

are simultaneously measured with two temperature-humidity sensors (Sensirion SEK-SHT35), as shown in Figure S2. The time constant of the sensors is about 8 s, thus we assume they acquire the real instantaneous hydrothermal characteristics of the airstream during adsorption and desorption phases, ~10 to 30 min. During data acquisition, the absolute humidity and the dew point at the measurement locations are concurrently calculated using the Arden Buck equation for the water vapor saturation pressure.[5] Figure S3 shows an image of the setup at Stanford Microfluidics Laboratory.

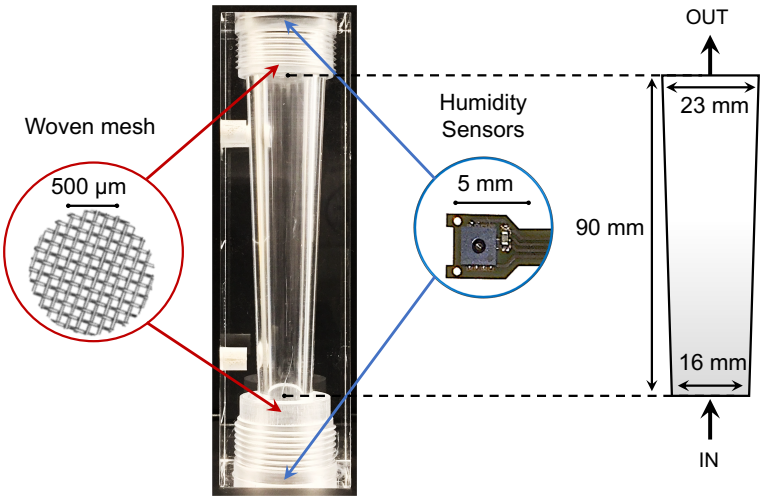

Figure S2. Further experimental details of the fluidized bed
Flow is upward through the divergent channel. Image shows fluidized bed empty of absorbent. Shown also are the locations (and a detailed view) of humidity-temperature sensors, as well as an image and locations of the two stainless steel woven meshes used as flow distributor (bottom) and powder retention filter (top).

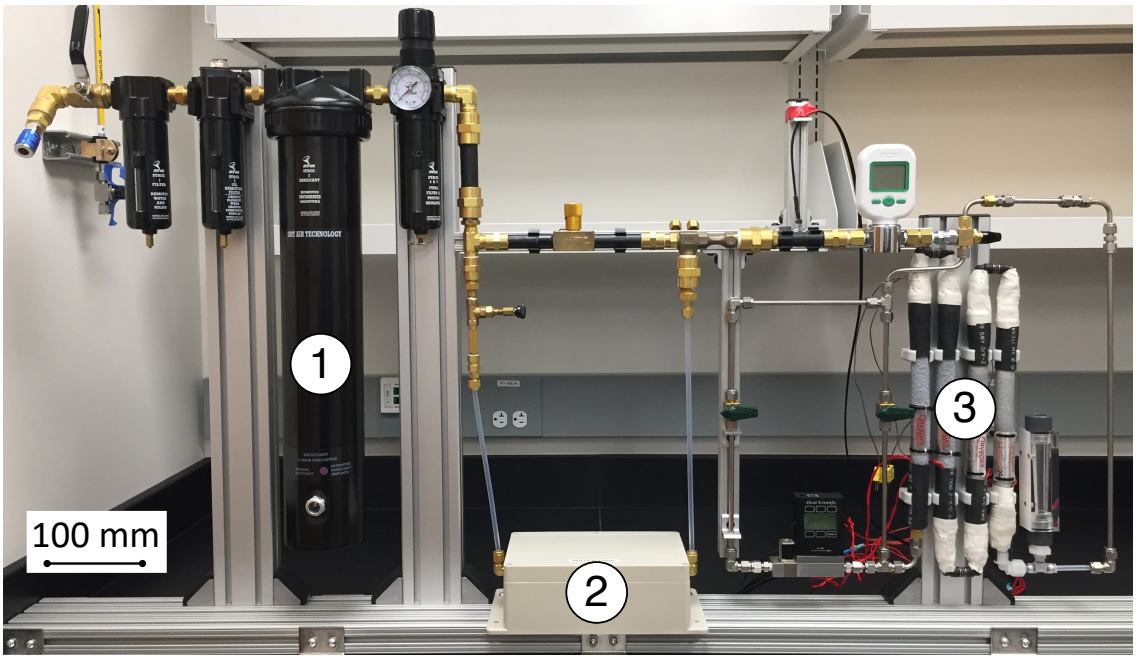

Figure S3. The continuous-cycled moisture harvesting test rig at Stanford Microfluidics Laboratory
Highlighted in the image are the desiccant dryer (1), the humidification unit (2) and the electrical heater (3). Inlet air enters from the left at the blue connection (shown here without inlet air hose). The fluidized bed is the right-most component above the T-junction compression fitting (bed chamber shown here empty).

Section 2: Characterization of powdered MOF-801

The crystal diameter of the powdered MOF-801 material was characterized by scanning electron microscopy (SEM) imaging. Typical crystal diameters (smallest characteristic length scale) vary between about 0.2 and 0.6 μm, with an average value of about 0.4 μm.

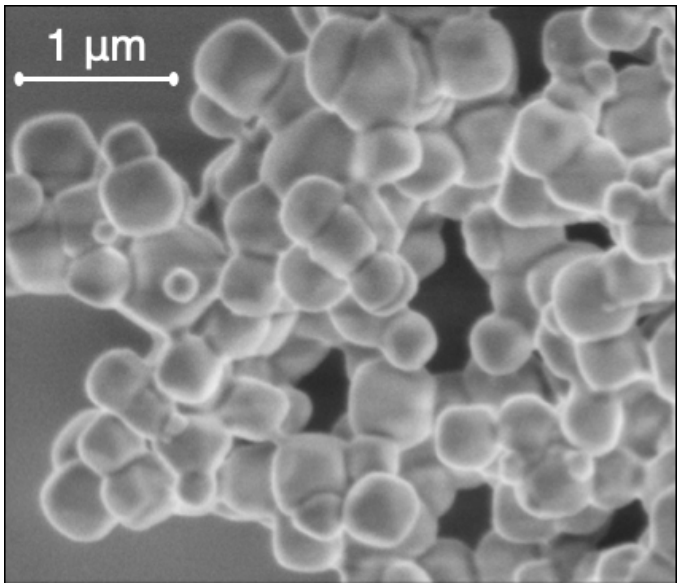

Figure S4. SEM images of the powdered MOF-801
An image processing analysis revealed an average crystal diameter of 0.4 μm.

Section 3: Instantaneous frames of MOF-801 fluidization

Figure S5 shows instantaneous fluidization images at various times over a water vapor adsorption and desorption cycle. In each row of images, consecutive frames are displayed at time intervals of 0.1 s. Four time periods are indicated: (a) near the beginning of adsorption process where MOF particles adsorb moisture (cold flow), (b) near the end of the adsorption phase where particles are nearly saturated (cold flow), (c) during the desorption phase where the particles release the captured water (hot flow), and (d) near the end of regeneration process where most the captured water has been released (hot flow).

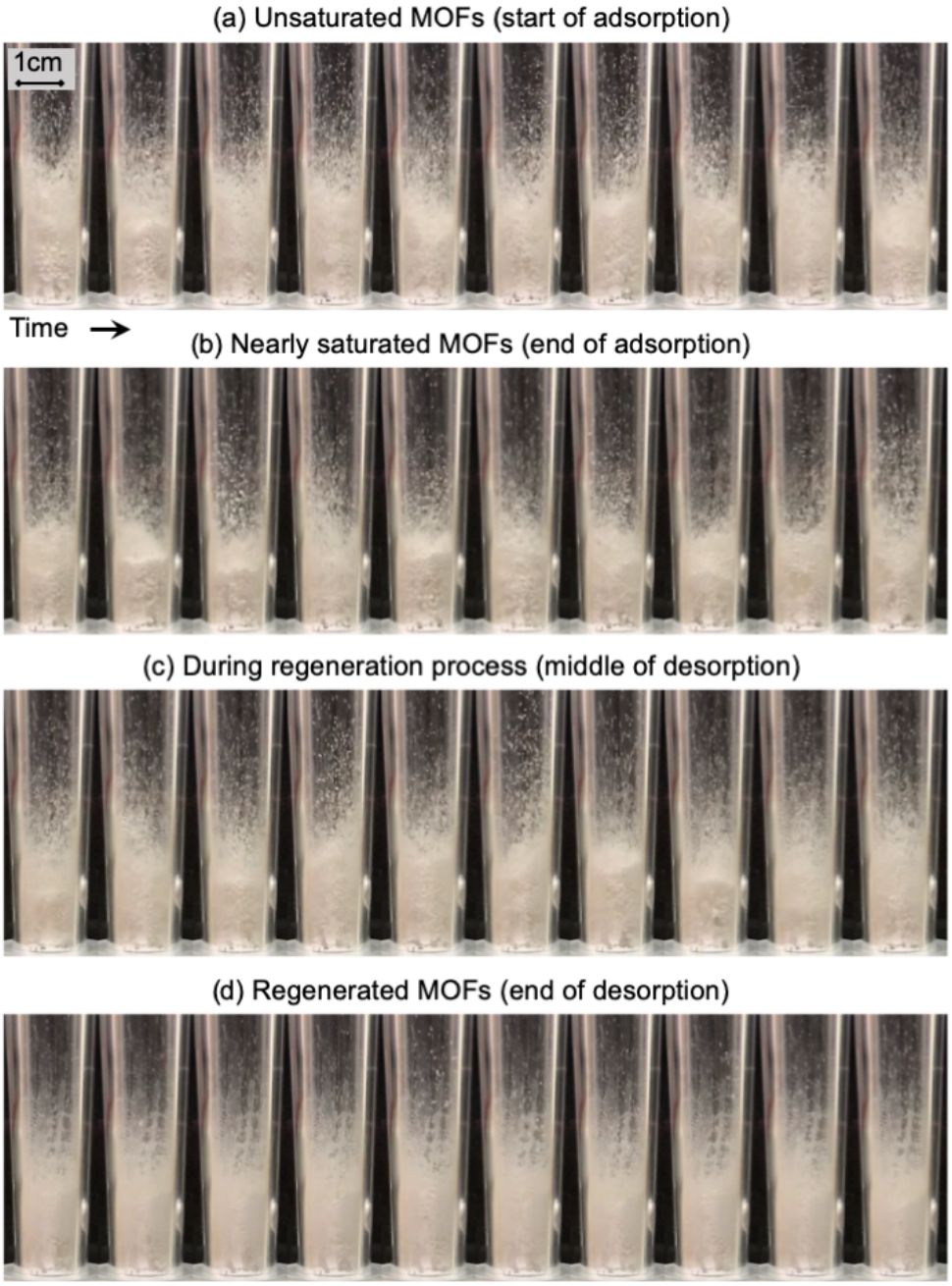

Figure S5. Instantaneous images at various instances during a water vapor adsorption and desorption cycle
Consecutive frames are displayed every 0.1 s to show the fast particle motion and uniform bubbling fluidization. The splashing zone at the top of the bed is characterized by upward ejection of small particles and up to 3 times the bed expansion while larger MOF-801 agglomerates are fluidized closer to the bottom of the bed. Note that there is a noticeable variation of bed expansion associated with water adsorption. We noticed that the agglomerates are smallest and more actively fluidized (e.g. to higher heights) near the beginning of adsorption process. Near the end of adsorption, by contrast, there is a noticeable shift of particles toward the bottom of the bed. At the end of desorption phase, we noticed that particles are reduced in size and stick on the acrylic vessel walls. Videos of the fluidized bed are also attached as Supplementary Information online.

Supplemental Notes

Section 4: Calculation of characteristic transport numbers

In the main text, we presented estimates of characteristic non-dimensional parameters for mass and heat transport in and out of any form of fluidized MOF-801 porous agglomerates, a. For this, we considered thermal (α) and mass (D) diffusion coefficients for transport within the heterogeneous network of intercrystalline voids spaces and the single MOF-801 crystals, as depicted in Figure S6. All thermophysical properties of MOF-801 crystals are based on literature values. In particular, we estimate a characteristic Lewis numbers for the MOF-801 crystals, the inter-crystalline void spaces and we also estimate an effective value for the whole agglomerate. For the two latter, we also estimate characteristic Péclet numbers for mass (Pe_c) and heat transfer (Pe_θ). Tables S1, S2 and S3 summarize the variables and equations used in our calculations.

For a given agglomerate porosity ε_a, the effective intercrystalline diffusivity D_v is calculated in analogy to tortuous porous media considering both molecular (D_{air}) and Knudsen diffusion (D_K).[6,7] Although D_K can be neglected at high porosity values, we expect a contribution of such term since the very small MOF-801 crystal diameters result in small characteristic pore spaces. We approximate the spacing between adsorbent crystals with the assumption of a close-packing of equal spheres. For a porosity of 0.72 (see **Observed fluidization dynamics and quantification of agglomerate distribution** in manuscript) and a crystal radius of 0.2 μm (see **Section 2**), we use a probability distribution as per Ref.[8,9] to estimate an average void radius (r_v) of 0.085 μm. The intercrystalline diffusivity D_v is then calculated to be 6.2E-7 m^2/s (see Table S1). Intracrystalline diffusivity of MOF-801 crystals has been measured using dynamic water uptake experiments. These published studies[9,10] report diffusivity values between 1E-17 and 1E-16 m^2/s, showing significant scatter with temperature and relative humidity (see Table S2). This value is about 9 orders of magnitude smaller than D_v and hence diffusion through solid is negligible compared to diffusion through the agglomerate (which is governed by mass diffusivity, D_a; see Table S3). That is, diffusion through such agglomerates is likely dominated by diffusion through air spaces.

The thermal diffusivity of intercrystalline voids (α_v) was estimated based on the thermophysical properties of air. For the MOF-801 crystals, density[9-10], specific heat[9,11-13] and thermal conductivity[14,15] values from open literature sources were considered. We know of no accurate values for MOF-801 specific heat and thermal conductivity. As a rough estimate, we considered published values for similar Zirconium-based metal-organic frameworks, e.g. UiO-66, which has similar molecular structure.[16,17] For the effective (e) agglomerate properties, we use a simple volumetric fraction in the form $\varphi_e = (1-\varepsilon_a)\varphi_c + \varepsilon_a\varphi_v$ since the ratio of crystal-to-voids thermal conductivity and specific heat is less than 100[18], see Tables S1 and S2.

The fluidized-MOF-801 porous agglomerates have an average radius of 4.0E2 μm and a high porosity of 0.72 (see **Observed fluidization dynamics and quantification of agglomerate distribution** in manuscript). The Reynolds number based on the average agglomerate diameter (d_a) and for a fluidization velocity of 0.3 m/s is about 15, which is well above creeping flow regimes. Given these estimates, we hypothesize a portion of airstream flows through their bodies[19], and we assume this scales with the fluidization velocity (0.3 m/s).

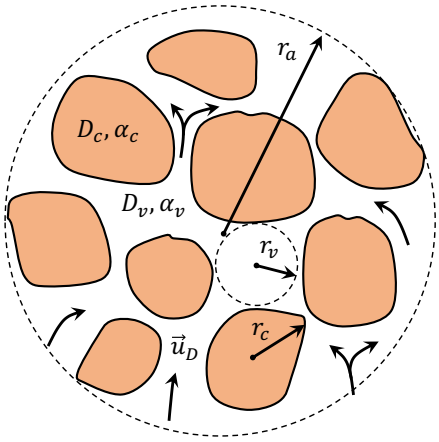

Figure S6. Geometrical characteristics of fluidized porous agglomerates
The simplified schematic that highlights voids (v) and MOF-801 crystals (c). Arrows indicate the possibility of an intercrystalline advective term that contributes to the mass and heat transport processes.

Table S1. Estimated thermophysical parameters for void spaces (filled with air) within agglomerates

Variable	Functional Form	Units	Value
d_v	$2r_v$	µm	0.17
ρ_v		$\mathrm{kg\ m^{-3}}$	1 – 1.22
k_v		$\mathrm{W\ (mK)^{-1}}$	0.025 – 0.03
$c_{P,v}$		$\mathrm{kJ\ (kgK)^{-1}}$	1
D_{air}	$f(T)$	$\mathrm{m^2\ s^{-1}\ (\times 10^{-5})}$	2 – 4
D_K	$\frac{d_v}{3}\sqrt{8\hat{R}T/\pi M}$	$\mathrm{m^2\ s^{-1}\ (\times 10^{-6})}$	~ 1
D_v	$\varepsilon_a^{3/2}\left(\frac{1}{D_{air}}+\frac{1}{D_K}\right)^{-1}$	$\mathrm{m^2\ s^{-1}\ (\times 10^{-7})}$	6.2
α_v	$\frac{k_v}{\langle \rho c_p \rangle_v}$	$\mathrm{m^2\ s^{-1}\ (\times 10^{-5})}$	2.25
u_D		$\mathrm{m\ s^{-1}}$	< 0.3
$Pe_{v,c}$	$\frac{u_D r_a}{D_v}$	[-]	> 1
$Pe_{v,\theta}$	$\frac{u_D r_a}{\alpha_v}$	[-]	> 1
Le_v	$\frac{\alpha_v}{D_v}$	[-]	~ 35

Table S2. Estimated MOF-801 crystal thermophysical parameters

Variable	Functional Form	Units	Value
r_c		µm	0.2
ρ_c [9-11]		$\mathrm{kg\ m^{-3}}$	~ 1400
k_c [14-15]		$\mathrm{W\ (mK)^{-1}}$	0.1 – 0.2
$c_{P,c}$ [9,11-13]		$\mathrm{J\ (kgK)^{-1}}$	780 – 980
D_c		$\mathrm{m^2\ s^{-1}\ (\times 10^{-17})}$	1 – 10
α_c	$\frac{k_c}{\langle \rho c_p \rangle_c}$	$\mathrm{m^2\ s^{-1} (\times 10^{-7})}$	~ 1.25
Le_c	$\frac{\alpha_c}{D_c}$	[-]	≫ 1

Table S3. Estimated thermophysical parameters for agglomerates

Variable	Functional Form	Units	Value
ε_a		[-]	0.72
r_a		μm	395
ρ_a		kg m^{-3}	390
k_a	$(1-\varepsilon_a)k_c + \varepsilon_a k_v$	W $(mK)^{-1}$	0.03 – 0.07
$c_{P,a}$	$(1-\varepsilon_a)\langle c_p \rangle_c + \varepsilon_a \langle c_p \rangle_v$	kJ $(kgK)^{-1}$	950
D_a	$\sim D_v$	$m^2\ s^{-1}$ $(\times 10^{-7})$	6.2
α_a	$\frac{k_a}{\langle \rho c_p \rangle_a}$	$m^2\ s^{-1} (\times 10^{-7})$	~ 1.4
$Pe_{a,c}$	$\frac{u_D r_a}{D_a}$	[-]	> 1
$Pe_{a,\theta}$	$\frac{u_D r_a}{\alpha_a}$	[-]	> 1
Le	$\frac{\alpha_a}{D_a}$	[-]	0.2 – 0.4

SUPPLEMENTAL REFERENCES

[1] Tashtoush, B. M., Al-Nimr, M. A., & Khasawneh, M. A. (2019). A comprehensive review of ejector design, performance, and applications. *Applied Energy*, 240, 138–172

[2] Gernon, T. M., & Gilbertson, M. A. (2012). Segregation of particles in a tapered fluidized bed. *Powder Technology*, 231, 88–10

[3] Bussière, W., Rochette, D., Clain, S., André, P., & Renard, J. B. (2017). Pressure drop measurements for woven metal mesh screens used in electrical safety switchgears. International Journal of Heat and Fluid Flow, 65, 60–72

[4] Geldart, D., & Baeyens, J. (1985). The design of distributors for gas-fluidized beds. *Powder Technology*, 42(1), 67–78

[5] Buck, A. L. (1981). New equations for computing vapor pressure and enhancement factor. *Journal of Applied Meteorology*, 20(12), 1527–1532

[6] Narayanan, S., Yang, S., Kim, H., & Wang, E. N. (2014). Optimization of adsorption processes for climate control and thermal energy storage. *International Journal of Heat and Mass Transfer*, 77, 288–300

[7] Moldrup, P., Olesen, T., Gamst, J., Schjønning, P., Yamaguchi, T., & Rolston, D. E. (2000). Predicting the Gas Diffusion Coefficient in Repacked Soil Water-Induced Linear Reduction Model. *Soil Science Society of America Journal*, *64*(5), 1588–1594

[8] Alonso, M., Sainz, E., Lopez, F. A., & Shinohara, K. (1995). Void-size probability distribution in random packings of equal-sized spheres. *Chemical Engineering Science*, *50*(12), 1983–1988

[9] Kim, H., Yang, S., Rao, S. R., Narayanan, S., Kapustin, E. A., Furukawa, H., et al. (2017). Water harvesting from air with metal-organic frameworks powered by natural sunlight. *Science*, 356(6336), 430–434

[10] Kim, H., Rao, S. R., Kapustin, E. A., Zhao, L., Yang, S., Yaghi, O. M., & Wang, E. N. (2018). Adsorption-based atmospheric water harvesting device for arid climates. *Nature Communications*, 9(1), 1191

[11] LaPotin, A., Kim, H., Rao, S. R., & Wang, E. N. (2019). Adsorption-Based Atmospheric Water Harvesting: Impact of Material and Component Properties on System-Level Performance. *Accounts of Chemical Research*, 52(6), 1588–1597

[12] Mu, B., & Walton, K. S. (2011). Thermal Analysis and Heat Capacity Study of Metal–Organic Frameworks. *The Journal of Physical Chemistry* C, 115(46), 22748–22754

[13] Kloutse, F. A., Zacharia, R., Cossement, D., & Chahine, R. (2015). Specific heat capacities of MOF-5, Cu-BTC, Fe-BTC, MOF-177 and MIL-53 (Al) over wide temperature ranges: Measurements and application of empirical group contribution method. *Microporous and Mesoporous Materials*, 217, 1–5

[14] Huang, B. L., Ni, Z., Millward, A., McGaughey, A. J. H., Uher, C., Kaviany, M., & Yaghi, O. (2007). Thermal conductivity of a metal-organic framework (MOF-5): Part II. Measurement. *International Journal of Heat and Mass Transfer*, 50(3-4), 405–411

[15] Huang, J., Xia, X., Hu, X., Li, S., & Liu, K. (2019). A general method for measuring the thermal conductivity of MOF crystals. I*nternational Journal of Heat and Mass Transfer*, 138, 11–16

[16] Furukawa, H., Gándara, F., Zhang, Y.-B., Jiang, J., Queen, W. L., Hudson, M. R., & Yaghi, O. M. (2014). Water Adsorption in Porous Metal–Organic Frameworks and Related Materials. *Journal of the American Chemical Society*, 136(11), 4369–4381.

[17] Ma, D., Han, G., Peh, S. B., & Chen, S. B. (2017). Water-Stable Metal–Organic Framework UiO-66 for Performance Enhancement of Forward Osmosis Membranes. *Industrial & Engineering Chemistry Research*, *56*(44), 12773–12782

[18] Zhao, C. Y. (2012). Review on thermal transport in high porosity cellular metal foams with open cells. *International Journal of Heat and Mass Transfer*, 55(13-14), 3618–3632

[19] Jain, A. K., & Basu, S. (2011). Flow Past a Porous Permeable Sphere: Hydrodynamics and Heat-Transfer Studies. *Industrial & Engineering Chemistry Research*, 51(4), 2170-2178